CrossMark

Stabilizing air dampers for hovering aerial robotics: design, insect-scale flight tests, and scaling

Sawyer B. Fuller[1,2,3] · Zhi Ern Teoh[2,3] · Pakpong Chirarattananon[4] · Néstor O. Pérez-Arancibia[5] · Jack Greenberg[6] · Robert J. Wood[2,3]

Abstract Most hovering aircraft such as helicopters and animal-inspired flapping-wing flyers are dynamically unstable in flight, quickly tumbling in the absence of feedback control. The addition of feedback loops can stabilize, but at the cost of additional sensing and actuation components. This can add expense, weight, and complexity. An alternative to feedback is the use of passive mechanisms such as aerodynamic drag to stabilize attitude. Previous work has suggested that small aircraft can be stabilized by adding air dampers above and below the center of mass. We present flight tests of an insect-scale robot operating under this principle. When controlled to a constant altitude, it remains stably upright while undergoing cyclic attitude oscillations. To characterize these oscillations, we present a nonlinear analytic model derived from first principles that reproduces the observed behavior. Using numerical simulation, we analyze how changing damper size, position, mass, and midpoint offset affect these oscillations, building on previous work that considered only a single configuration. Our results indicate that only by increasing damper size can lateral oscillation amplitude be significantly reduced, at the cost of increased damper mass. Additionally, we show that as scale diminishes, the damper size must get relatively larger. This suggests that smaller damper-equipped robots must operate in low-wind areas or in boundary-layer flow near surfaces.

✉ Sawyer B. Fuller
  minster@uw.edu

  Zhi Ern Teoh
  zhiernteoh@seas.harvard.edu

  Pakpong Chirarattananon
  pakpong.c@cityu.edu.hk

  Néstor O. Pérez-Arancibia
  perezara@usc.edu

  Jack Greenberg
  jack.d.greenberg@gmail.com

  Robert J. Wood
  rjwood@seas.harvard.edu

[1] Department of Mechanical Engineering, University of Washington, Seattle, WA 98195, USA

[2] School of Engineering and Applied Sciences, Harvard University, Cambridge, MA 02138, USA

[3] The Wyss Institute for Biologically Inspired Engineering, Harvard University, Boston, MA 02115, USA

[4] Department of Mechanical and Biomedical Engineering, The City University of Hong Kong, Kowloon, Hong Kong

[5] Department of Aerospace and Mechanical Engineering, University of Southern California, Los Angeles, CA 90089, USA

[6] Google, Inc., Mountain View, CA 94043, USA

1 Introduction

A number of challenges confront an engineer designing an autonomous insect-sized aerial vehicle. Machine elements such as motors, bearings, and airfoils become inefficient as they get smaller because surface effects become increasingly important relative to inertial, Newtonian forces (Trimmer 1989). This is because the ratio of surface area to volume increases with decreasing scale. For example, viscous forces become increasingly important relative to lift-generating aerodynamic inertial forces. The smallest flying animals such

as hummingbirds and flies have adapted to this by continually flapping their wings to generate lift, rather than gliding like larger animals (Dudley 2002; Dickinson et al. 1999). This is because flapping may be more efficient than fixed-wing gliding for small animals (Wang et al. 2004; Pesavento and Wang 2009). Other examples include a higher relative strength per mass of coulomb friction, and decreasing efficiency of the electromagnetic fields in electric motors due to greater thermal dissipation in small magnetic coils (Trimmer 1989). These changes suggest that actuation, aerodynamics, and flight control may all require different approaches from what has been used successfully in larger aircraft.

Despite these challenges, developing aerial insect robots is motivated by their capability to perform tasks not possible with other robots. They combine small size, aerial mobility, reduced human safety hazard, and minimal materials usage, permitting large numbers to be deployed at low cost. Applications that could benefit include search and rescue, robot-assisted agriculture monitoring, chemical detection and source localization, reconnaissance, and home monitoring.

Previous work in small-scale aerial vehicles has supported the view that new approaches are needed in actuation and flight control. The very lightest aerial vehicles powered by electromagnetic motor, such as the Delfly Micro (De Croon et al. 2009) or 3D printed ornithopter (Richter and Lipson 2011), have been limited to about 3 g and above. Other examples include a 75 g spinning robot modeled after a samara leaf (Ulrich et al. 2010), a 19 g robot resembling a hummingbird (Keennon et al. 2012), as well as early efforts to make a tiny autonomous helicopter (Kroo and Kunz 2000). Switching to a rubber band as a power source can allow mass to diminish even further, reaching as low as 390 mg for a butterfly-inspired ornithopter (Tanaka and Shimoyama 2010). But adding perception for feedback control would require incorporating an additional electronic power source. Another alternative to electromagnetic motors for tiny insect-scale flight was first seriously proposed by Ron Fearing, who suggested using piezoelectric actuators to drive a "micro-robotic flying insect" or MFI, that is actuated by tiny flapping wings (Fearing et al. 2000; Wood et al. 2003). Piezo actuators are driven by electrostatic forces rather than magnetic forces, whose efficiency and power density do not diminish nearly as fast with decreasing scale (Trimmer 1989). Subsequent advances have included a laser-based fabrication process for insect-scale composite structures that are articulated using flexure joints (Wood et al. 2008), leading to the first lift-to-weight ratio greater than one for a fly-sized robot (Wood 2008). With the addition of a second actuator so that the wings could be independently actuated (Ma et al. 2012), this led to the first controlled maneuvers in free flight (Ma et al. 2013).

To reduce cost and complexity, particularly as the scale reduces to that of insects, it is desirable to simplify the flight apparatus as much as possible. For example, an early microrobotic flying insect prototype was unable to lift its own weight because of the complexity of its wing-driving mechanics (Wood et al. 2003). Constructed to re-create the lift-producing wing kinematics of hovering insects (Ellington et al. 1996; Dickinson and Götz 1996), it employed two actuators for each wing to actively control both degrees of freedom and a sophisticated spherical five-bar linkage. The result, however, was that much of the power output of the actuators was used to drive the system away from its natural dynamics. This led to low efficiency and a system that was too heavy to lift its own weight. The solution, proposed later (Wood 2008), was to drastically simplify the mechanism by allowing it to follow its natural dynamics. Each wing's angle of attack was instead allowed to rotate passively around an elastic flexure joint and only the wing's stroke angle was actuated. The result was that the system's inherent dynamics produced similar wing motions to those of hovering insects using much less power and weight, producing the first fly-sized mechanism able to lift its own weight (Wood 2008). In a later example of using mechanics to reduce the need for active feedback, a differential-like mechanism was introduced (Sreetharan and Wood 2011) that could compensate for design irregularities. For example, if a portion of one wing was damaged, this mechanism's mechanics would cause it to flap it at a larger amplitude to compensate.

Here we consider another example of using passive dynamics to simplify the design of insect-sized aerial vehicles. Specifically, we are concerned with the stability of the robot's attitude while in flight. When first flown without guide wires, the the robotic fly quickly tumbled to the ground after lifting off (Pérez-Arancibia et al. 2011). Like many flying insects, its center of mass hangs below the wings (Ellington 1984), and this is thought to lead to dynamic instability about rotational axes (Ristroph et al. 2013; Fuller et al. 2014b). One approach to compensate for this, and stabilize to an upright orientation, is to use a sensor in an active feedback loop. In insects, sensors that are thought to measure rotation for this purpose include the gyroscopic halteres of flies (Pringle 1948; Ristroph et al. 2010; Dickinson 1999), vibrating antennae in moths (Sane et al. 2007), and possibly the light-sensing ocelli at the top of the head (Wilson 1978; Fuller et al. 2014b). In human engineered systems, gyroscopic feedback has been used to stabilize unstable systems such as fighter jets (Abzug and Larrabee 2002) and robot flies (Fuller et al. 2014a). Other approaches include an external camera-based motion-capture system and reflective markers mounted on the vehicle (Ma et al. 2013), an ocelli-inspired sensor (Fuller et al. 2014b), or a magnetometer (Helbling et al. 2014). However, incorporating any of these sensors implies tradeoffs. For example, power usage could increase, the possible domains of application could be restricted, or, most significantly, the addition

of sensors could add complexity, increasing the chance of failure.

Taking inspiration from earlier work described above in which improved mechanical design improved performance, we consider here incorporating air dampers to passively stabilize flight. This work is inspired by earlier hovering robots that were stabilized upright using air dampers placed both above and below the center of mass, consisting of either dampers and large wings themselves in the case of the Mentor robot (Zdunich et al. 2007) or air dampers above and below the center of mass in addition to wings (van Breugel et al. 2008; Richter and Lipson 2011). The basic principle is that the aerodynamic center of pressure must be located above the center of mass, causing a self-righting torque that stabilizes the upright orientation during hovering (Fig. 2). Note that this configuration for stability at hover is opposite to what is needed for stability in forward flight. For the latter, the center of mass must be positioned ahead of the center of aerodynamic pressure (Zdunich et al. 2007). The benefit of using dampers rather than a sensor-actuator loop for stability is that this can simplify the flight system.

Like the work reported here, previous work has combined empirical and physics-based models to understand the behavior of this system. (Zdunich et al. 2007) used an aerodynamic simulator to model their aircraft to help in design, but little information is given about the the model. (Richter and Lipson 2011) appears to use an entirely empirical design process, while (van Breugel et al. 2008) shows stability by linearizing flight dynamics at an operating point with a small ($\theta = 10°$) attitude inclination.

This paper aims to provide a more comprehensive characterization of these flight dynamics of damper-equipped robots using simple analytic models and numerical simulation, along with data from flight tests. This paper extends the results of an earlier report (Teoh et al. 2012). We start by deriving a model for the dynamics of a damper-equipped, insect-sized vehicle from wind tunnel tests (Sect. 3). From this model, we derived a simplified, linear model, and used this model to design a prototype robot. We then fabricated the prototype shown in Fig. 1, which weighed approximately 100 mg. We then flew this robot in a motion capture arena to control its altitude to a fixed value so that its dynamic behavior could be measured (Sect. 5). The results show that during all flights, the robot undergoes cyclic oscillations which are not predicted by the linear model. A more elaborate and accurate nonlinear model exhibits limit cycle behavior when simulated numerically (Sect. 6). The nonlinearity arises from aerodynamic drag on the dampers, which varies quadratically with airspeed. The paper concludes with an analysis of how the cyclic behavior of this dynamical system varies as parameters are changed. Our key contributions are (1) a demonstration of passive aerodynamic stability on an insect-scale robot, where simplicity is of paramount importance,
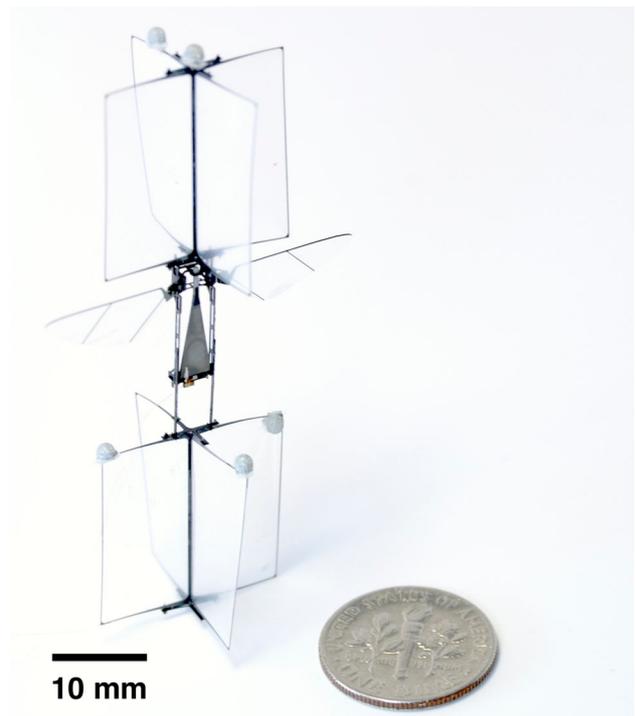
Fig. 1 Image of the robotic fly equipped with 20 mm stabilizing air dampers. The small *white spheres* attached to the dampers are retroreflective markers used to track the vehicle's motion using external cameras. A U.S. 10-cent coin is shown for scale

(2) a nonlinear model and analysis of the damper-equipped robot that reveals how different parameters affect dynamic behavior.

2 Design considerations

Our analysis indicates that stability at hover using dampers requires two key elements (Fig. 2):

1. The aerodynamic center of pressure must be above the center of mass to cause a self-righting torque during lateral motion
2. There must be sufficient rotational drag to prevent overrotation

To achieve these ends, the dampers are oriented vertically at hover to produce aerodynamic drag during lateral motion. For robots of the scale of interest here, i.e. roughly insect-scale, our results indicate that this requires locating one above and the other below the center of mass (CM) to have a sufficiently large rotational damping. This is consistent with the findings for hovering robots at larger scales (Zdunich et al. 2007; van Breugel et al. 2008; Richter and Lipson 2011). Ramifications for changing damper size and distance are discussed in Sect. 3.
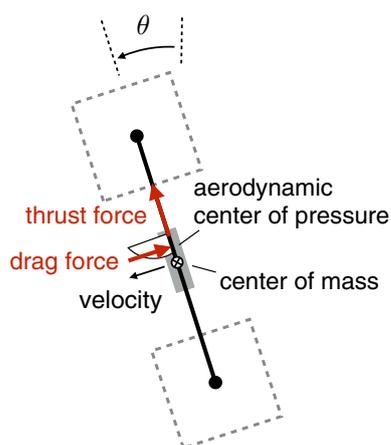
Fig. 2 How dampers provide a restoring torque to maintain upright stability. As the vehicle inclines (θ), the thrust force (produced for example by flapping wings) takes on a lateral component, accelerating the vehicle to the side. As the vehicle moves sideways, aerodynamic drag force begins to act. If the aerodynamic center of pressure lies above the center of mass, then a net torque arises that acts to return the vehicle to an upright orientation. Additionally, rotational damping is needed to prevent over-rotation. This is achieved by moving the dampers a distance away from the center of mass to increase the moment-arm

We choose square dampers, rather than, for example, circular ones, because our structural elements are made from unidirectional carbon fiber composites arranged in a 0–90–0° layup. Therefore, structural elements not aligned with the fibers are comparatively weak, suggesting rectilinear shapes for optimum performance. Rectangular shapes are not as area-efficient as squares for producing drag.

Our analysis is only concerned with equally-sized dampers at the top and bottom because we believe that unequal-sized dampers does not represent a path to improved performance. Differently-sized dampers could be used to move the aerodynamic center of pressure away from their midpoint. But our analysis shows that the distance needed between the center of pressure and CM is very small (1–3 mm) relative to the distance needed between the dampers (30–100 mm) to add sufficient rotational drag. So there is little need for additional means to move the center of pressure further.

3 Model

In this section we describe a model of an insect-sized, damper-equipped flying robot. The goal of the model is to predict the behavior of the robot so that guidelines can be found for damper configuration, such as their size and distance from the center of mass. Damper design ultimately involves a number of tradeoffs which include weight, overall size, fragility, and susceptibility to wind gusts. Because of this, we do not attempt to specify an optimal design, but rather attempt to provide the reader with design guidelines to help choose the right balance.

3.1 Aerodynamic drag

We start by considering how drag on a vertically-oriented flat-plate damper, as depicted in Fig. 1, acts on the robot as it moves laterally through the air (Fig. 2). For lateral motions on the order of 1 m/s (Ma et al. 2013), the Reynold's number $Re = \rho v l / \mu$ is 1300 for a damper with area $A = 400$ mm^2 (length $l = 20$ mm), where $\rho = 1.2$ kg/m^3 is the density of air near sea level and $\mu = 18 \times 10^{-6}$ Ns/m^2 is the viscosity of air. Therefore, at the scale and speeds of interest, approximately those of insects, drag in this flow regime is dominated by inertial, rather than viscous forces. A model for drag in this regime is that it varies quadratically with airspeed according to

$$f = \rho A C_d v |v|, \tag{1}$$

where v is the velocity of the impinging flow, A is the area of the damper, and C_d, known as the drag coefficient, accounts for shape- and flow-dependent effects (Hoerner 1965). The $v|v|$ component respects the squared dependence on drag but preserves the correct sign.

To confirm the validity of the model and find the correct C_d for our damper shape, we measured drag for our damper designs for wind speeds ranging from 0.0 to 1.0 m/s in a wind tunnel (Engineering Laboratory Design, Lake City, MN, USA). The wind speed was monitored by a hot-wire anemometer and regulated with a proportional-integral-derivative (PID) controller to achieve precise control. This feedback loop provided a steady-state accuracy of ± 0.01 m/s. We mounted the damper at the end of a 30 cm moment arm attached to a precision six-axis force–torque sensor (Nano17 Titanium, ATI Industrial Automation, Apex, NC, USA). Torque readings from the sensor were measured after the wind velocity had reached a steady state and converted to force by dividing by the length of the moment arm. This provided a resolution of 27 μN (2.8 mg) with a range of ± 30 mN. The mounting arm was also subject to aerodynamic drag, so its effect was measured separately beforehand and subtracted out.

We measured forces on three square damper sizes, 15, 20 and 30 mm. We additionally consider smaller 10 mm dampers in this work, but the test shape for that size produced forces too small to be measured with sufficient precision using our sensor. Accordingly for that size we extrapolated our results, which are consistent with well-established fluid drag relations (Hoerner 1965). Force measurements sizes are shown in Fig. 3. A least-squares fit of Eq. (1) to the data found that $C_d = 0.43$ ($R^2 = 0.99$). This compares to an estimate of $C_d = 0.58$ measured for a square flat plate for $Re \gtrsim 1000$ (Hoerner 1965) (p. 3–15). Note that the drag on a flat plate is reduced by approximately 16% if a second plate is attached perpendicular to it on the downstream side
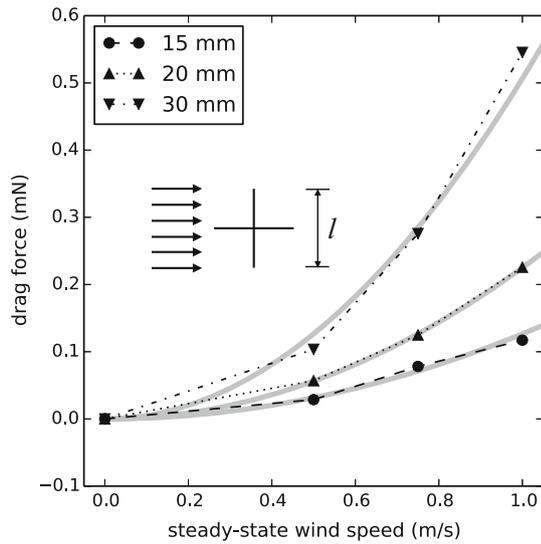
Fig. 3 Drag force on passive air dampers mounted transverse to the flow of air in a wind tunnel. (*Inset*) As seen from above, air flow in the tunned moved perpendicularly to the cross-shaped damper. The drag force follows the prediction of Eq. (1), varying quadratically with wind speed and linearly with damper area. A least-squares fit to the data gives an estimated drag coefficient C_d in Eq. (1); predicted drag forces with this factor are shown in *grey*

that "splits" eddies in the downstream wake (Hoerner 1965) (p. 3–7), predicting a reduced C_d of 0.5, which is close to our estimate. The cross-shaped arrangement of the dampers shown in Fig. 1 consists of the same perpendicular two-plate configuration. The measured C_d also compares closely to the value of 0.44 that was estimated by fitting free-flight data (Chirarattananon and Wood 2013).

We also considered the drag acting on the thruster mechanism for the specific case of flapping wings. As above, we performed wind tunnel tests on a flapping-wing prototype. We found that aerodynamic drag is almost perfectly proportional to velocity, as shown in Fig. 4, following $f_d = -b_d v$, where b_d is the slope coefficient, or, equivalently, the damping constant and v is the velocity through the fluid. In that figure it is also shown that if the vehicle is rotated $90°$ about its vertical (z-) axis so that the wind is blowing laterally across it rather than head-on, drag also approximates a nearly identical linear function. We do not have an aerodynamic model to explain why lateral drag is roughly equal to frontal drag, but remark that it simplifies analysis because both pitch and roll motions can therefore be modeled by the same dynamics.

3.2 Rigid body dynamics

We describe the dynamics of the body of the vehicle using the following equations of motion:

$$\dot{\boldsymbol{\theta}} = \boldsymbol{W}(\boldsymbol{\theta})\,\boldsymbol{\omega}, \tag{2}$$
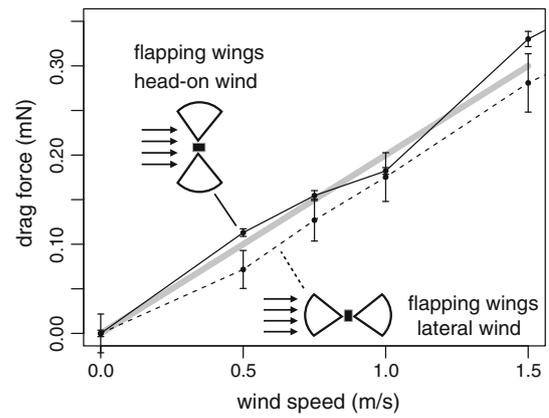
Fig. 4 Drag arising from flapping wings is roughly linear with airspeed and is roughly equal for motion along either the x or y axis. (*Inset*) Wind impinging from head-on (along x-axis) and laterally (y-axis). The linear approximation for both directions was fitted by least-squares and is shown by a *thick line*

$$\mathbf{J}\,\dot{\boldsymbol{\omega}} = \boldsymbol{\tau} - \boldsymbol{\omega} \times \mathbf{J}\,\boldsymbol{\omega}, \tag{3}$$

$$\dot{\boldsymbol{p}} = \boldsymbol{R}(\boldsymbol{\theta})\,\boldsymbol{v} \tag{4}$$

$$m\,\dot{\boldsymbol{v}} = \boldsymbol{f} - \boldsymbol{\omega} \times m\,\boldsymbol{v}, \tag{5}$$

where $\boldsymbol{\theta} \in SO(3)$ is the vehicle's attitude and is represented by an array of three Euler Angles $\boldsymbol{\theta} \doteq [\theta_1, \theta_2, \theta_3]^T$; $\boldsymbol{v} \in \mathbb{R}^3$ is the velocity of the vehicle's center of mass (CM); $\boldsymbol{\omega} \in \mathbb{R}^3$ is its angular velocity about the CM; $\boldsymbol{\tau} \in \mathbb{R}^3$ is the sum of all torques or moments applied to the body, primarily aerodynamic forces and control torques generated by the wings; $\boldsymbol{f} \in \mathbb{R}^3$ is the sum of external forces acting on the CM; $m \in \mathbb{R}^1$ is the mass; and $\mathbf{J}$ is the vehicle's moment of inertia. The position $\boldsymbol{p}$ is given in inertial, Earth-fixed coordinates; all other vectors are expressed in body-attached coordinates. With this parameterization, the moment of inertia becomes a matrix $\mathbf{J} \in \mathbb{R}^{3 \times 3}$, as does the rotation matrix $\boldsymbol{R}(\boldsymbol{\theta}) \in SO(3)$. Euler Angles have singularities at extreme attitudes but the representation is convenient to describe motion in the neighborhood of a certain attitude. We parameterize Euler Angles in zyx-order: the attitude is obtained by first rotating by an angle θ_3 (yaw) around the body z-axis, then by θ_2 (pitch) around the new body y-axis, and then by θ_1 (roll) around the new body x-axis. Therefore, the rotation matrix, which transforms body-attached coordinates to Earth-fixed coordinates, takes the form

$$\boldsymbol{R} = \begin{bmatrix} c\theta_2 c\theta_3, & s\theta_1 s\theta_2 c\theta_3 - s\theta_3 c\theta_1, & s\theta_1 s\theta_3 + s\theta_2 c\theta_1 c\theta_3 \\ s\theta_3 c\theta_2, & s\theta_1 s\theta_2 s\theta_3 + c\theta_1 c\theta_3, & s\theta_2 s\theta_3 c\theta_1 - s\theta_1 c\theta_3 \\ -s\theta_2, & s\theta_1 c\theta_2, & c\theta_1 c\theta_2 \end{bmatrix},$$

where we have used the shorthand c for cos and s for sin. The quantity $\boldsymbol{W}(\boldsymbol{\theta}) \in \mathbb{R}^{3 \times 3}$ is a matrix that relates the angular velocity $\boldsymbol{\omega}$ to the rate of change in Euler Angles $\dot{\boldsymbol{\theta}}$ so that Eq. (2), written in terms of coordinates, is given by:

$$\begin{bmatrix} \dot{\theta}_1 \\ \dot{\theta}_2 \\ \dot{\theta}_3 \end{bmatrix} = \begin{bmatrix} 1 & \sin\theta_1 \tan\theta_2 & \cos\theta_1 \tan\theta_2 \\ 0 & \cos\theta_1 & -\sin\theta_1 \\ 0 & \sin\theta_1/\cos\theta_2 & \cos\theta_1/\cos\theta_2 \end{bmatrix} \begin{bmatrix} \omega_1 \\ \omega_2 \\ \omega_3 \end{bmatrix}. \quad (6)$$

Torques $\boldsymbol{\tau}$ are all derived from forces $\boldsymbol{f}$ and are written as the cross product of a position vector $\boldsymbol{d}$ relative to the CM and $\boldsymbol{f}$ according to

$$\boldsymbol{\tau} = \boldsymbol{d} \times \boldsymbol{f}. \quad (7)$$

3.2.1 Inertial and gravitational masses

Bodies undergoing acceleration in a fluid move a portion of the fluid with them, which can be modeled as an additional mass known as "fluidic added mass" (Sane and Dickinson 2001; Blevins 2015). In one-dimensional form, the force balance including added mass can be expressed simply as additional mass in the system:

$$\Sigma f = (m + m_a)\,\dot{v},$$

where m_a is the added mass. The amount of added mass depends on the shape and cross-sectional area of the moving body exposed to the fluid flow. In (Blevins 2015) (Table 6.7) are tabulated added mass models for different shapes. For damper motions in the body x- and y-directions, the cube shape in that table is closest to the square-shaped dampers considered in this report. Note that added mass does not depend on the thickness of an object, so a square plate moving perpendicular to the flow and a cube moving with its face perpendicular to the flow are expected to have equivalent added mass. For a cube with a side length of l, the relation is

$$m_a = 0.64\rho l^3, \quad (8)$$

where ρ is the density of the fluid flow. Using $\rho = 1.2\,\text{kg/m}^3$ (the density of air at sea level), this gives an estimate of $m_a = 6.1$ mg for a damper of length $l = 20$ mm. Compared to the mass of that damper itself, 16 mg, added mass therefore represents a non-negligible component of a damper's inertia.

We remark that our added mass model does not take into account the effect of downwash flow from the wings. Gravish et al. (2015) reports flow velocity measurements of the downwash from a flapping wing of our design by particle image velocimetry (PIV) and hot-wire anemometer. It shows that above the wings, average flow is negligibly small, <0.01 m/s. Below the wings, the flow is larger, but also likely negligible because it flows outward. It averages approximately 0.1 m/s at a distance of ≈20 mm (the typical distance to the bottom damper considered here), compared to a root mean squared value of 0.22 m/s for the dampers themselves in the flight experiments in Sect. 4. But peak flow is concentrated near the tip of the wing and flows outward away from the dampers at

an angle approximately 30° away from the negative z-axis, so little of this flow reaches them. Nonetheless we believe a more thorough analysis of this specific phenomenon, such as by computational fluid dynamics simulation, could yield a more accurate model of flight dynamics.

To incorporate the effect of added mass on our model, we note that added mass affects inertia but not gravity. Accordingly, we make a distinction between gravitational and inertial masses. For the full 3D case, we define $m \in \mathbb{R}^1$ to be the gravitational mass, and introduce $\mathbf{m}_I \in \mathbb{R}^{3\times3}$, a diagonal matrix that compactly represents the direction-dependent inertia that is the result of fluidic added mass.

With inertial mass, the force balance Eq. (5) is rewritten so that momentum is described as the product of inertial mass and velocity:

$$\mathbf{m}_I \dot{\boldsymbol{v}} = \Sigma \boldsymbol{f} - \boldsymbol{\omega} \times (\mathbf{m}_I \boldsymbol{v}),$$

and we note that the gravitational force acts on the gravitational mass m according to

$$\boldsymbol{f}_g = \boldsymbol{R}^T [0,\ 0,\ -mg]^T.$$

The total gravitational mass is

$$m = m_t + m_1 + m_2,$$

where m_t is the mass of the thrusting or flapping mechanism and m_1 and m_2 are the masses of the top and bottom dampers, respectively. We have neglected the mass of the damper supports because it is very small (Sect. 4.1). The inertial mass is given by a diagonal matrix

$$\mathbf{m}_I = \text{diag}\left(m + m_{ax},\ m + m_{ay},\ m\right),$$

where $m_{ax} = m_{ay}$ are the fluidic added masses for the body x- and y-axis directions. We model added mass along the z-direction as negligible because of the very small cross-sectional area exposed to flow in that direction, and neglect off-diagonal terms.

The moment of inertia is affected by fluidic added mass as well. The robot—and its added mass—is symmetric about all three of its orthogonal coordinate axes, so its moment of inertia takes the form $\mathbf{J} = \text{diag}(J_{xx}, J_{yy}, J_{zz})$. About the body x- and y-axes, the moment of inertia is approximately the same. Assuming that the thruster's moment of inertia is J_t, the total moment of inertia about the CM for these two axes is (using the parallel axis theorem):

$$J = J_t + m_t d_t^2 + J_1 + (m_1 + m_a)\,d_1^2 + J_2 + (m_2 + m_a)\,d_2^2,$$

where d_t is the distance from the CM to the center of mass of the thruster mechanism (Fig. 5). We model the square,
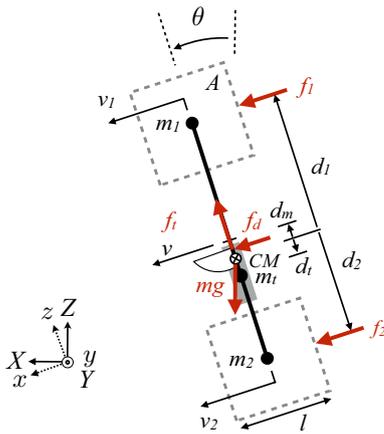
Fig. 5 Diagram of forces acting on the robot (*red*) and parameters (*black*). The robot has mass m whose center is at the CM (Center of Mass). The CM moves with velocity v, given in body-attached coordinates. Body-frame and world-frame coordinate systems are shown as *dashed arrows* in inset at *lower left*, which are rotated relative to each other by the vehicle's inclination angle θ (*top*). The robot is subject to a thrust force f_t produced by wings or propellors, gravitational force mg, and aerodynamic drag acting on the two dampers f_1 and f_2 and the thruster f_d. The locations of the *top* and *bottom* dampers relative to the CM are d_1 and d_2, respectively. Note that $d_1 > 0$ and $d_2 < 0$. The midpoint of the pair of dampers (shown as a *tick mark* on main beam connecting dampers, also known as the aerodynamic center of pressure) is located d_m from the CM. The center mass of the lift-generating thruster is at d_t from the CM. The velocities of these two dampers in body-attached coordinates are v_1 and v_2. Each square damper has area A and dimension l given by its length (Color figure online)

cross-shaped dampers as cubes, for which there is a simple relation for the moment inertia about their center of mass of, $J = \frac{1}{6}ml^2$.

Note that our analysis assumes that the inertial and gravitational centers of masses are coincident for notational simplicity. This is because in practice their relative displacement is negligible (≈ 0.2 mm). But the effect could be incorporated by adding an additional gravity-induced torque.

3.2.2 Simplified planar dynamics model

We will show that the relevant dynamics can be simplified to a much lower order system that considers only motion in the plane. This will facilitate analysis. To do so, we use a number of assumptions that hold for the case considered here:

1. ω_3, the angular velocity about the body z- or vertical axis is small;
2. θ_1 and θ_2 are small;
3. the inertia matrix is diagonal; and
4. v_3 is small.

The consequence of assumption 1 can be seen by writing Eq. (3) in component form,

$$J_{xx}\dot{\omega}_1 = \tau_1 - (J_{zz} - J_{yy})\omega_2\omega_3$$
$$J_{yy}\dot{\omega}_2 = \tau_2 - (J_{xx} - J_{zz})\omega_1\omega_3$$
$$J_{zz}\dot{\omega}_3 = \tau_3 - (J_{yy} - J_{xx})\omega_1\omega_2.$$

This reduces to $J\dot{\omega} = \tau$ around the first and second axis for for small ω_3. The consequence of assumption 2 is that W in Eq. (6) reduces to the identity matrix. And because of assumptions 1 and 2, the terms appearing in the cross product $\omega \times m\,v$ in Eq. (5) are small for the first two axes, as can be shown by writing out the cross product terms. The equation therefore reduces to $m_1\dot{v} = f$ for the first and second components of v. The result of these realistic simplifying assumptions is that the θ–v_1 (pitch-heave) dynamics are decoupled from the (θ_1 to v_2) roll-sway dynamics, and can be considered independently. For pitch-heave heave dynamics, the equations of motion can therefore be written as

$$\dot{\theta} = \omega$$
$$J\dot{\omega} = \Sigma\tau$$
$$\dot{p} = v\cos(\theta)$$
$$m_1\dot{v} = \Sigma f. \tag{9}$$

A similar relation holds for roll-sway dynamics.

As an additional test to confirm that this simplification to a 2D planar model represented an accurate representation of the full 3D dynamics, we compared our 2D nonlinear simulation of these dynamics (used in the analyses of Sect. 6) against a second simulator that computed the full three-dimensional rigid-body motion of a damper-equipped system. The second simulation was written in a different language, MATLAB instead of python, to minimize duplicate errors in the simulation code. The prediction of the simplified model (Eq. 9) agreed with the full simulation to within 10% for all three state variables for general conditions of nonzero vertical motion (breaking assumption 4), while both pitch and roll dynamics were excited (breaking assumption 2), as well as for when $\omega_3 \neq 0$ (breaking assumption 1). This indicates that the model with simplifying assumptions given above is an adequate representation of the full three-dimensional behavior of this system.

3.2.3 Forces

The total force including damper and thruster drag in the body x-direction is $\Sigma f = f_1 + f_2 + f_d + f_g$, where f_g is the force due to gravity. The gravity force is for the planar dynamics case is

$$f_g = mg\sin\theta. \tag{10}$$

Now we consider how drag on the dampers is induced by motion of the vehicle. Figure 5 shows a diagram of the vehi-

cle's damper configuration and forces acting on it. Flat-plate theory indicates that the aerodynamic force on the dampers is almost entirely due to the component of flow perpendicular to its surface (Hoerner 1965). This can be written in vector format as $f = \rho A C_d v_\perp |v_\perp|$, where f is the drag force vector and $v_\perp$ is the component of the flow velocity v that is perpendicular to the surface of the damper. This simplifies our analysis, allowing the velocity (along the x-axis) to be written as $v_{1\perp} = d_1\omega + v$ for the top damper and $v_{2\perp} = d_2\omega + v$ for the bottom damper, where ω is the angular velocity of the vehicle about its CM along its body y-axis and v is its velocity along its x-axis. Note that $d_1 > 0$ and $d_2 < 0$.

We assume aerodynamic drag is equal across the damper and that it acts at its center. For this approximation to hold, the distance from the damper to the vehicle's center of mass must be much larger than its length l, which generally holds here. Below, we revisit this assumption using data taken from flights and simulation to show that flow due to rotational motions about the center of each damper is much lower than that due to translational motions and motions around the of the entire vehicle. Aerodynamic forces on the top and bottom damper are thus approximated by

$$f_1 = -\rho l^2 C_d (d_1\omega + v) |d_1\omega + v| \quad \text{and}$$
$$f_2 = -\rho l^2 C_d (d_2\omega + v) |d_2\omega + v|, \tag{11}$$

respectively, where the damper area $A = l^2$.

As in the case of the dampers, the drag resulting from vehicle motion acting on the wings is thus

$$f_d = -b_d(d_d\omega + v), \tag{12}$$

where d_d is the distance from the CM to the center of aerodynamic drag pressure acting on the wings (or propeller or other thrusting mechanism) and b_d is its damping coefficient.

3.2.4 Torques

The total torque on the vehicle about its y-axis is $\Sigma\tau = \tau_1 + \tau_2 + \tau_d + \tau_g + \tau_p$. The quantity τ_p is a torque disturbance perturbation we consider the effect of later. Such a perturbation could be caused by for example asymmetry in the flapping system that causes one wing to flap with greater force than the other. Torques along the y-axis resulting from forces can be found using Eq. (7) and are given by

$$\tau_1 = d_1 f_1$$
$$\tau_2 = d_2 f_2$$
$$\tau_d = d_d f_d$$
$$\tau_g = 0. \tag{13}$$

Note that the torque due to gravity is zero because gravity acts at the center of mass CM.

Note that the dampers also induce torque as they rotate about their centers, but this effect is negligible. In the flight experiments in Sect. 4, the root mean square velocity of the midpoint of the dampers themselves was approximately 0.22 m/s, while the outer edge of each damper moves with a root mean squared velocity of only 0.05 m/s relative to its center. With a velocity-squared dependence on drag, this additional torque therefore represents at most a 20× factor less than the torque induced by rotation and translation of the entire vehicle, and so we neglect this contribution.

3.3 Linearized model

We first considered a linearization of the dynamics of the damper-equipped robot (Eqs. 9–13), taken around $\theta = \omega = v = 0$. To linearize damper drag to have the form $f = -bv$, we took a least-squares linear regression on drag force data (Fig. 3) for airspeeds up to 1.0 m/s. This gave damping coefficients for 20 mm dampers of $b = 1.8 \times 10^{-4}$ Ns/m. Similarly, for the wings, which behave almost linearly in both frontal and lateral flow, $b_d = 2.0 \times 10^{-4}$ Ns/m. We also take the small-angle approximation of $\sin\theta \approx \theta$.

To provide insight into how different parameters affect stability, we simplified the analysis by choosing parameters that allow convenient term cancellations. We choose identical top and bottom dampers ($b_1 = b_2 = b$) equidistant from the CM ($d_1 = -d_2 = d/2$). In this case, we rely on drag on the wings to move the center of aerodynamic pressure above the CM. Writing out all of the terms in Eq. (9), neglecting position because it does not act on the system's dynamics, gives

$$\dot{\theta} = \omega$$
$$\dot{\omega} = \frac{1}{J}\left[\left(-bd^2/2 - b_d d_d^2\right)\omega - b_d d_d v\right]$$
$$\dot{v} = \frac{1}{m}\left[mg\theta + -b_d d_d\omega + (-2b - b_d)v\right]$$

To assess the stability of this system, we cast it in the form of a state-space system according to $\dot{q} = Aq$, where the state vector is $q = [\theta, \omega, v]^T$ and A is the so-called state-transition matrix. The dynamics of this system are stable if all of the eigenvalues of A have negative real parts. The Routh–Hurwitz stability criterion can be used to determine this by analyzing the characteristic equation $\det(A - \lambda I) = 0$, which is a polynomial of the form $a_3\lambda^3 + a_2\lambda^2 + a_1\lambda^1 + a_0 = 0$. It states that stability is assured if and only if all $a_k > 0$ and $a_2 a_1 > a_3 a_0$. All of the $a_k > 0$ by inspection since mass and inertia must be positive and non-zero, so the stability criterion reduces to

$$\frac{2b}{Jm^2} \left[(2b + b_d)\, d^2/4 + b_d d_d^2 \right]$$
$$\times \left[(2b + b_d)\, J + \left(b_d d_d^2 + bd^2/2 \right) m \right]$$
$$> b_d d_d g. \tag{14}$$

Assuming b_d and d_d are fixed by the flapping mechanism, this equation indicates that there are two clear paths to achieve stability for the linearized dynamics. First, the criterion can be satisfied if the factor b/Jm^2 is made large enough, which can be achieved by increasing b by increasing damper area. Second, note that inside the left pair of brackets of Eq. (14), we can neglect $b_d d_d^2$ since $(2b + b_d)\, d^2/4 \gg b_d d_d^2$ because the distance from the dampers to the CM is much larger than from the wings to the CM ($d/2 \gg d_d$). This indicates that increasing d will also bring the system closer to stability.

Based this linear analysis, we chose to equip our experimental robot platform with $l = 20$ mm dampers, separated by $d = 40$ mm, with $d_d = 3.9$ mm. The robot is shown in Fig. 1. This configuration represented a good compromise between manufacturability and flight weight (larger dampers are more difficult to make and heavier) and robust stability.

4 Design and fabrication

Because our focus was on attitude stability, we performed flight tests on a simple flapping mechanism consisting of only a single power actuator for simplicity, based on the design that demonstrated vertical flight control in (Pérez-Arancibia et al. 2011). This design cannot actuate in the roll direction, so its lateral position is not under feedback control and is allowed to drift slowly. The rate is slow enough that sufficient data can nevertheless be collected about its performance.

Dampers were fabricated out of a frame of 80 μm thick unidirectional carbon fiber, cured from prepreg out of three plies arranged at 0°–90°–0° orientations and machined using a 355 nm diode-pumped solid state laser (Wood et al. 2008; Whitney et al. 2011). Each damper consists of two interlocking surfaces that form a cross. The cross is fixed on both ends by caps that lock the dampers with respect to each other. The aerodynamic surface of the damper is made from a sandwich of two sheets of 1.5 μm polyester. Before sandwiching, the polyester is stress relieved at its glass transition temperature 150 °C for 1 min twice. Next, the sandwich is put in between a layup of four layers of Teflon on either side to limit adhesion, a 3 mil steel sheet and a kapton/silicone/kapton layer on each side of the sandwich to distribute forces evenly. The layup is put under 3.6 MPa of pressure and heated to 150 °C for 15 min and is left to cool under pressure. Under these conditions, the polyester membranes self-adhere, encapsulating the carbon fiber frame between them. Once cooled, the outline of the damper is laser cut to release the damper from the sandwich. Some additional detail can be found in (Teoh et al. 2012).

4.1 Physical dimensions of damper supports

We briefly address the practical matter of translating theoretical parameters into physical dimensions of parts on the robot. The motivation is driven by how, in practice, as the location of the midpoint between the dampers varies relative to the mass of the thrusting mechanism, the location of the CM varies, depending on the relative masses of different components. Therefore there is not a straightforward relation between part dimensions and physical locations d relative to the CM.

To find these dimensions, we introduce a second coordinate system defined relative to the center of mass of the thrusting or flapping mechanism, with positions denoted by r parameters. Coordinates in this r frame represent the dimensions of physical parts, whereas d parameters are positions relative to center of mass CM of the entire damper-equipped vehicle. Our aim is to, given component masses m_t, m_1, and m_2, and desired damper distances d_1 and d_2 or the position of their midpoint d_m, compute r_1, and r_2, or the position of their midpoint r_m, which specify these positions relative to the thruster's center of mass.

Define r_m to be the distance from the thruster's center of mass to the midpoint between the dampers. In the CM coordinate frame we define d_m as the position of the midpoint of the dampers, and d_t as the distance to the center of mass of the thruster, as shown in Fig. 5. Then by geometry,

$$d_t = d_m - r_m. \tag{15}$$

We then use the definition of the center of mass to write

$$m_{I1} d_1 + m_{I2} d_2 + m_t d_t = 0. \tag{16}$$

Note that we neglect the effect of mass of the structure to support the damper at a distance from the robot because constitutes a negligible fraction of the total mass and moment of inertia of the vehicle. For example, a 10 mm extension has a mass of only 1 mg, or about 1% of the robot. Then, substituting Eqs. (15) into (16), we find that $r_m = m_I d_m / m_t$. Then, defining the distance between dampers as $d = d_1 - d_2$, we have that $r_1 = d/2 + r_m$ and $r_2 = -d/2 + r_m$. Similarly, it can be shown that $d_1 = d/2 + d_m$ and $d_2 = -d/2 + d_m$. Note that we use m_I to denote *inertial* mass (see Sect. 3.2.1).

5 Flight tests

To test the operation of the dampers in flight, we implemented a feedback system to regulate its altitude to a constant value.

We used a motion capture system consisting of a set of external cameras (Vicon T040-series, Oxford, UK). The cameras' position and orientation are calibrated with respect to each other, allowing them to triangulate the position of reflective markers attached to the vehicle. During each frame, each camera emits a flash of infrared light from light emitting diodes. An imager records the location of reflections. Four cameras were positioned approximately 60 cm apart, close enough to detect five 1.5 mm spherical retroreflective markers weighing approximately 3 mg each attached to the vehicle (B & L Engineering, Santa Ana, CA, USA) over a volume approximately 45 cm across. The cameras take images at a frame rate of 500 Hz.

We used a desktop computer running XPC-target (a real-time operating system, MathWorks, Natick, MA) to perform control computations. This computer received pose information from the motion capture system over serial RS-232 connection. The feedback latency of this system is approximately 10–20 ms (Ma et al. 2013). The computer computed the response of a proportional-derivative (PD) controller at at 10 kHz and produced analog output voltages using a digital-to-analog board. These signals were then routed through a high-voltage amplifier (Trek, Lockport, NY, USA) and connected to the piezo actuator through a thin bundle of four 51-gauge copper wires. The mass of the wires, approximately 5 mg, is much less than that of the vehicle. In experiments, the actuators were driven with an amplitude of 230 V peak-to-peak. Before flying, we found the resonant frequency of the wing-actuator system by comparing the flapping amplitude measured by high speed video at different frequencies, choosing the frequency of maximum amplitude, which was approximately 105 Hz (Finio et al. 2011).

The altitude controller used a P gain of $K_p = 900$ V/m and D gain of $K_d = 210$ V/sm and was tuned based on simulations of a simple model of the robotic fly's vertical dynamics consisting of its mass, neglecting air drag. To this signal was added a baseline feedforward signal of 216 V that was found to be the minimum signal to achieve take-off. The derivative term was added to damp the dynamics and add phase lead. To minimize damage to the actuator and transmission, we limited the peak-to-peak voltage amplitude to an interval that ranged from 200 to 256 V. This controller was able to stabilize the robot's altitude with small error as shown in Fig. 6, and could regulate altitude at a number of different altitude setpoints as shown in Fig. 7.

In Fig. 8, plots of angular velocity versus attitude are given for the θ_1 and $\dot{\theta}_1$ for the three different trials shown in Fig. 7.

The results show the following. First, the attitude of the vehicle remains in a generally upright orientation, indicating that the dampers are successfully able to keep the vehicle from inverting and crashing, as occurs without the
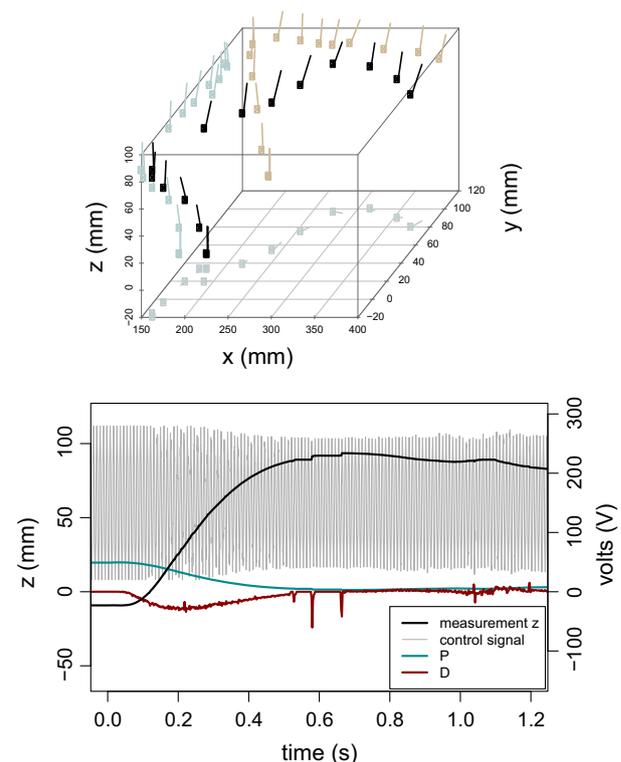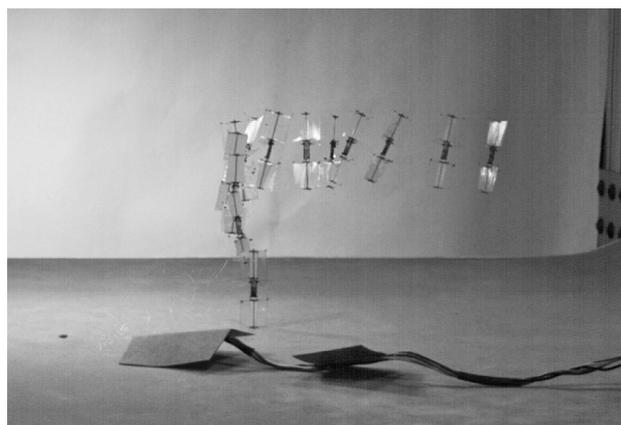
Fig. 6 High-speed videocomposite of altitude control of flapping-wing vehicle stabilized by air dampers. In this flight, the vehicle was controlled at an altitude of 100 mm (*top*). Here the robotic fly accelerates vertically until reaching an altitude setpoint, then begins to drift laterally. During the trial, we recorded the altitude measured by visual tracking (*bottom*, *left axis*), the P and D amplitude control commands, and piezoelectric actuator voltage during this trial run (*bottom*, *right axis*)

dampers (Pérez-Arancibia et al. 2011; Fuller et al. 2014b). Secondly, the attitude appears to undergo an oscillation. In all three flight tests, the attitude varies with an amplitude of approximately 20°–30° during the course of the flight, with angular velocity and attitude tracing out roughly circular motions in a phase-space plot (Fig. 8).
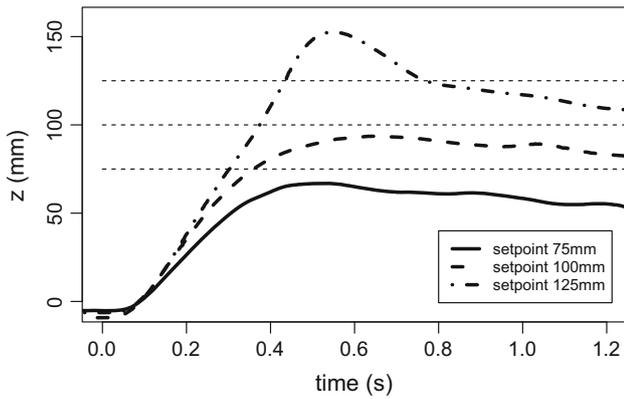
Fig. 7 Flight altitude during three flight tests recorded by motion capture cameras. The small error in the three cases is likely due to the steady-state error that can be manifested in a PD controllers, which do not have an integral term
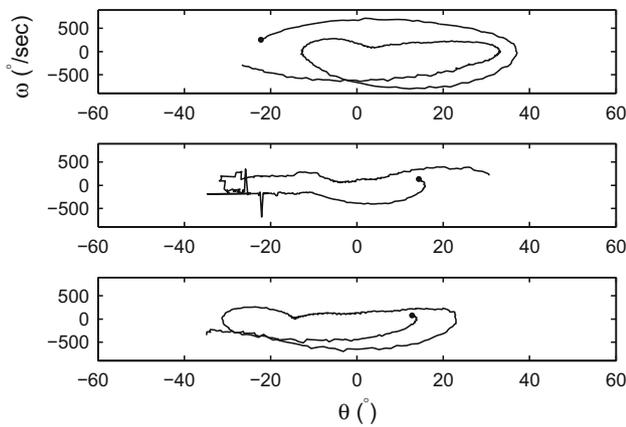
Fig. 8 Limit cycle plot of θ_1 (attitude) versus ω_1 (angular velocity) for the three three trials shown in Fig. 7. A dot denotes the start of a trial

6 Nonlinear model analysis

The linear model given in 3.3 was useful for providing a baseline set of design parameters, but the the attitude oscillations shown in Fig. 8 suggest that the robot does not eventually reach a stable equilibrium point as suggested by the linear analysis given in Sect. 3.3. The quadratic dependence on drag of our dampers (Sect. 3.1) is an inherently nonlinear phenomenon: at a lateral velocity in the neighborhood of zero, the drag is nearly zero.

To better understand the dynamics of this system it was necessary to perform a nonlinear analysis. Our first aim was to cast the equations of motion (Eqs. 9–13) into a form that permitted analytic treatment. But we were unable to distill the system's behavior into anything simpler. The authors welcome suggestions by researchers who may be aware of more advanced techniques in nonlinear analysis. Of particular interest would be formulations that are invariant with respect to scale.
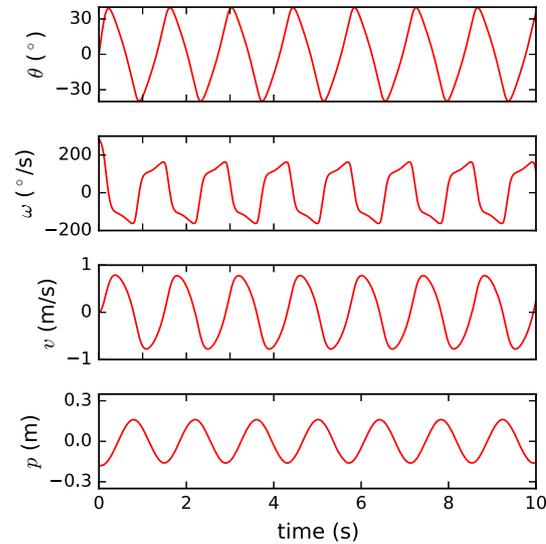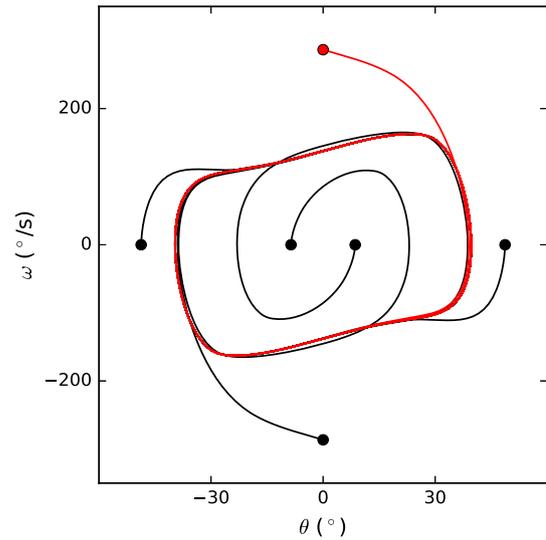
Fig. 9 Limit cycle for dampers. (*Top*) Regardless of initial state (shown as *dots*), trajectories of the system asymptotically become entrained in a cyclic pattern known as a "limit cycle." Note that the dynamics are three-dimensional, so paths can cross on a two-dimensional plot. (*bottom*) A single trajectory (shown in *red* above) is shown in terms of the three state variables plus the output position (Color figure online)

Accordingly, for this report we resorted to numerical simulation. We wrote the simulation in Python (version 3.5) using the Jupyter notebook and Scipy (version 0.12). Numerical integration was performed using a fixed-step integrator. The time step was chosen to be $dt = 2$ ms so that the simulation ran quickly while yielding predictions within 0.1% of those with an asymptotically smaller time step (0.01 ms). Figures 9 and 10 show the behavior of the system for parameters given in Table 1. We measured r_t, the distance from the thruster's center of mass to the center of drag of the wings (approximated by their leading edge, where the majority of the surface area is) by balancing a damper-free flapping mechanism on
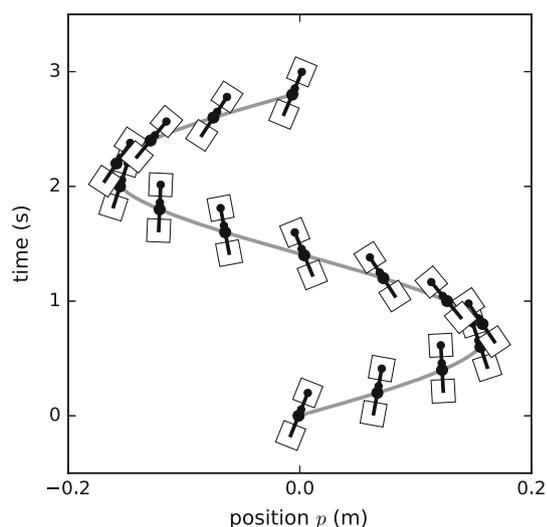
Fig. 10 Limit cycle behavior of the damper-equipped robot (Fig. 9) showing position and attitude snapshots at 0.1 s intervals. The position p of the *CM* (*grey line* and *large dots*) is plotted along the x-axis and evolves with time plotted on the y-axis

Table 1 Parameters used in the numeric simulation of the robot model in Figs. 9 and 10

Symbol	Name	Value	Units
C_d	Aerodynamic drag coefficient	0.43	N/A
b_d	Aerodynamic damping coefficient, wings	2.0×10^{-4}	N s/m
l	Damper length	20	mm
d	Distance between dampers	40	mm
d_m	Damper midpoint position relative to *CM*	-3	mm
m_1, m_2	Mass of 20 mm damper	16	mg
m_t	Mass of thruster mechanism	80	mg
J_t	Moment of inertia of thruster mechanism	1.5×10^{-9}	kg m^2
r_t	Position of wings relative to thruster center of mass	7	mm
τ_p	Torque perturbation disturbance	0.1×10^{-6}	N m

a sharp edge under a microscope. The moment of inertia of the flapping mechanism, J_t, was estimated using a computer aided design (CAD) model. The simulation of this system with these parameters resembles that observed in the three flight tests (Fig. 8).

The simulation indicates that, regardless of initial condition, the dynamics of the vehicle become entrained into a cyclic oscillation known as a "limit cycle" with a finite amplitude. Only in the limit of infinite damper length l or distance d does the oscillation magnitude reduce to zero.

Table 2 Parameters used for scaling damper mass and wing drag

Symbol	Name	Value	Units
k_m	Damper mass scaling	0.04	kg/m^2
k_t	Wing drag scaling factor	1.25×10^4	N s/(m kg)

6.1 Performance evaluation

In this section we use our simulation to analyze the system's behavior and provide design guidelines for hovering aerial vehicles. Recognizing that there are different goals to design, we used two criteria to evaluate the flight performance: (1) the size of oscillations, measured by amplitude of position and attitude oscillations, and (2) the degree to which the configuration was robust to a torque perturbation. The size of position oscillations is relevant when considering the size of confined spaces to fly through; the size of attitude oscillations may be important when considering onboard sensors such as cameras or magnetometers. For criterion (2), we measured to what degree the robot was affected by a non-zero disturbance torque τ_p, such as is caused by manufacturing irregularity in the flapping mechanism. A nonzero disturbance torque causes the vehicle to tilt, inducing a lateral velocity. A measure for the resistance of the vehicle to such disturbances is the size of the resulting lateral velocity. We measured this disturbance-induced lateral velocity by simulation, calculating the mean lateral velocity by averaging over a single cycle after it had reached a limit cycle or a steady-state inclination.

6.1.1 Wings-included model

We performed an analysis in which the drag effect of wings for our specific vehicle was incorporated. For this analysis, we relaxed the assumption of equidistant dampers ($d_1 = d_2$) used in the linear analysis of Sect. 3.3 to see what, if any, effect this has on the dynamics. To account for scaling effects, we additionally incorporated two scaling terms. The first was how the mass of the dampers scales with their length l. We assumed the mass of the dampers scales with their area[1]

---

[1] A detailed analysis suggests that if instead the damper is considered to be made of beams that must support the load of a impact landing, quadratic scaling is reasonable. We consider the damper support structure as a simply-supported beam. We neglect the mass of the polyester layer because it has similar density ($\approx$15 kg/m^3) to carbon fiber but a much lower thickness, at 3 μm compared to 80 μm for the carbon fiber composite. Assume the maximum force the beam is expected to support is F^*, caused by, for example, crash landings. Then the greatest moment applied to the beam of length l occurs at its base, and is equal to $M^* = F^* l$. Suppose the beam has a width w and thickness t
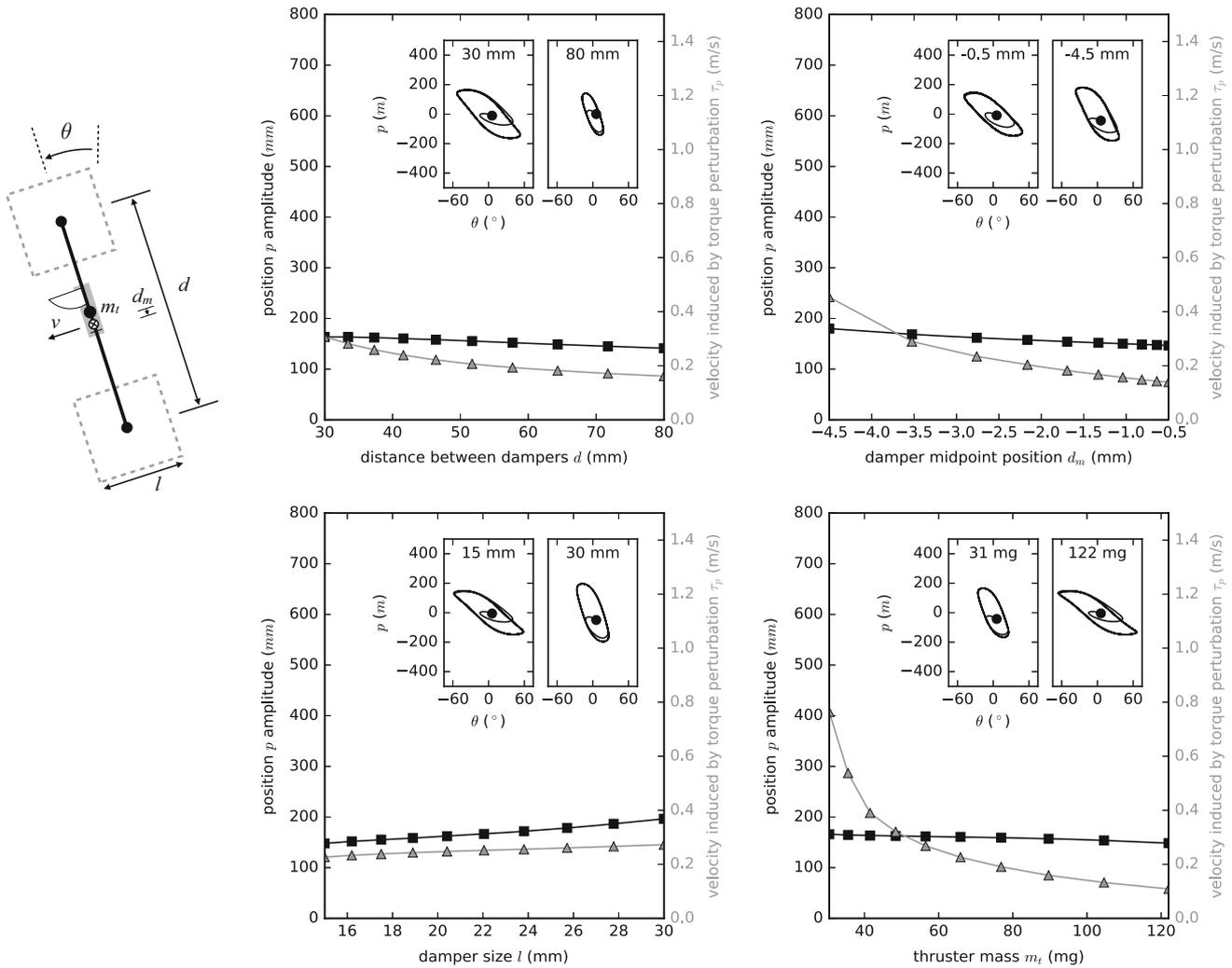
Fig. 11 Wings-included model: how varying different parameters affects the amplitude of oscillations. (*Top left*) Diagram of parameters that are varied. (*Top middle*) Position amplitude remains constant (*Black squares*) as damper distance increases, though attitude oscillations are reduced. (*Inset*) This occurs because, as damper distance increases, the time of period of each oscillation increases. (*Top right*) Varying the damper midpoint position has little effect on position amplitude.

(*Bottom left*) Increasing damper size reduces position oscillation, but this comes at the expense of increased weight. (*Bottom right*) Increasing thruster mass increases oscillation amplitude. (*All*) The effect of a torque disturbance. Increasing the damper midpoint position in the positive body z-direction or increasing damper size reduces the effect of torque disturbances. (*Grey triangles*) Other perturbations have a smaller effect

Footnote 1 continued

($\approx 80 \, \mu$ m for our material). Tensile stress inside the beam at its base is $\sigma = \frac{M^* y}{I}$, where $I = \frac{wt^3}{12}$ is the moment of inertia of the rectangular beam and y is the distance from its centerline. Then maximum stress σ^* in the material occurs at the top and bottom of the beam, and is equal to3 $\sigma^* = \frac{M^* t/2}{I}$.

Our interest is in a scaling law that, for a constant load F^* and material strength σ^*, gives the mass of the damper. Substituting the above equations into each other, we find that, for constant t (that is, a fixed fabrication process), the width of the beam must be $w = 6 \frac{F^*}{\sigma^*} \frac{l}{t^2}$. The mass of a single beam is $m = \rho l w t$, where ρ is the density of the material. Substituting, we find that the mass must be $m = 6\rho \frac{F^*}{\sigma^*} \frac{l^2}{t}$, or, written more succinctly, $m = k_m l^2$ for all other terms kept constant. To find the value of k_m, rather than compute these terms, we simply calibrate it to a damper design that, after a few iterations, has been found to support

according to $m = k_m l^2$. For a damper of length $l = 20$ mm, we measured the damper mass to be 16 mg using a precision scale. Using this value gives $k_m = 0.04 \, \text{kg/m}^2$ (Table 2). We additionally incorporated corresponding changes to moment of inertia into our simulation. Second, air drag on the wings varies with the amount of thrust produced: more thrust requires larger wings. To account for this, we introduce the wing thrust drag scaling factor k_t. We assumed that wing drag scales linearly with the flapping-wing thruster mass,

Footnote 1 continued

the necessary loads. In this case, the damper consists of many separate beams, all of which are of the same thickness of carbon fiber and must support similar loads.

neglecting the mass of the dampers, giving $b_t = k_t m_t$. We estimated its value by assuming a thruster mass of zero has zero drag, and that our flapping-wing thruster mass and drag factor were measured to have the values given in Table 1. This gives $k_t = 1.25 \times 10^4$ N s/(m kg) (Table 2).

Figure 11 shows how varying each of the parameters affects the amplitude of position oscillations. For each case, a single parameter is varied while all others are fixed at values given by Table 1. The results show that, for the wings-included case, all of the parameters that we varied have little effect on the amplitude of position oscillations. It is hard to provide an explanation of this phenomenology because it is a result of how the location of the aerodynamic center of pressure varies with airspeed: air drag on the wings acts in proportion to airspeed while drag on the dampers acts in proportion to the square of airspeed. This shows the need for numerical simulation. As observed in the insets, these perturbations do have an effect on the attitude oscillation amplitude, however. The reason this is not mutually exclusive is that the time period of the oscillations varies as well, which is not visible in the plots.

We also considered the effect of a small torque disturbance τ_p (Table 1). Increasing the damper midpoint position in the positive body z-direction and decreasing thruster mass increase the effect of torque disturbances. Other perturbations have a smaller effect.

Based on these results, we then inverted the problem, asking what parameters result in a desired oscillation amplitude. Given that there does not appear to be a means to alter position oscillations, we instead performed the analysis for attitude oscillations. We chose a target amplitude of 30°. As damper length l, distance d, and thruster mass m_t have the largest, effect, we chose to focus on those. We chose to find that damper distance d that results in the target desired oscillation amplitude for a given m_t and l. We performed a numerical optimization to search for the optimal value, minimizing the squared error using a Levenberg–Marquardt optimizer (`scipy.optimize.lstsq` in Python's Scipy package). Figure 12 shows the result of the analysis. The behavior resembles an exponential. To fit to an exponential function we used a multilinear least-squares exponential regression using the `scipy.optimize.curve_fit` command. The resulting relation giving the necessary damper length to achieve the desired amplitude of position oscillations is is given by

$$d = 0.20 m_t^{0.55} l^{-1.0},$$

where m_t is given in kg and l and d are given in m. This is shown by thin lines in the figure, showing good agreement. We observe that the necessary distance varies as the square root of mass and inversely with the size of the dampers. This
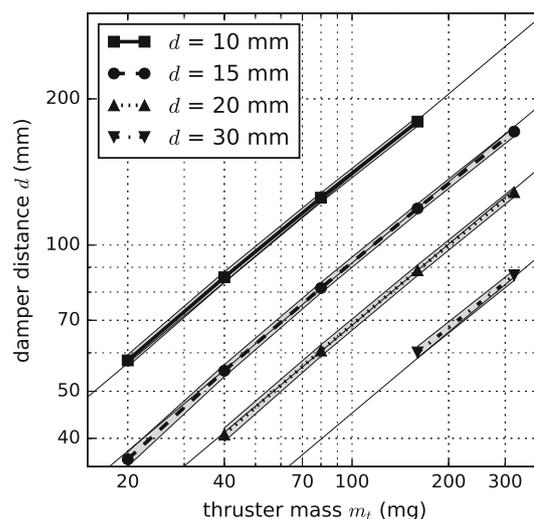
Fig. 12 Damper distances necessary to achieve a 30° oscillation amplitude. Plots in this figure include the effect of aerodynamic drag on the wings. *Shaded area* represents variability when amplitude is varied by $\pm 1°$. For cases in which the model gives a damper distance that is too small to be physically possible because of its size and the size of the flapping mechanism, data is not plotted

Table 3 Parameters that are different from Table 1 in the simulation of the wing-free damper model

Symbol	Name	Value	Units
d_m	Damper midpoint position	1.5	mm
J_t	Thruster moment of inertia	0	kg m^2
b_d	Thruster damping drag coefficient	0	N s/m

indicates that a quadrupling of vehicle mass requires doubling the damper distance or the damper length.

6.1.2 Wing-free model

Finally, to better understand basic scaling effects, we considered the behavior of a system that did not have the damping effect of the flapping wings. This is a simpler system with fewer assumptions, and it may be a better representation for other mechanisms of thrust generation such as propellors or rocket propulsion. These forms of thrust do not have the large moving surface area and therefore drag of flapping wings. Table 3 gives those parameters that are different from those used in Table 1.

The results show that position oscillation amplitude does not vary with damper distance d or midpoint offset d_m, but that increasing damper length l and reducing thruster mass m_t can reduce these oscillations. As can be seen in the insets of Fig. 13, perturbations that do not have an effect on position amplitude such as damper distance d and damper midpoint position d_m do change attitude oscillation amplitude. As above, this is possible because these perturbations vary the
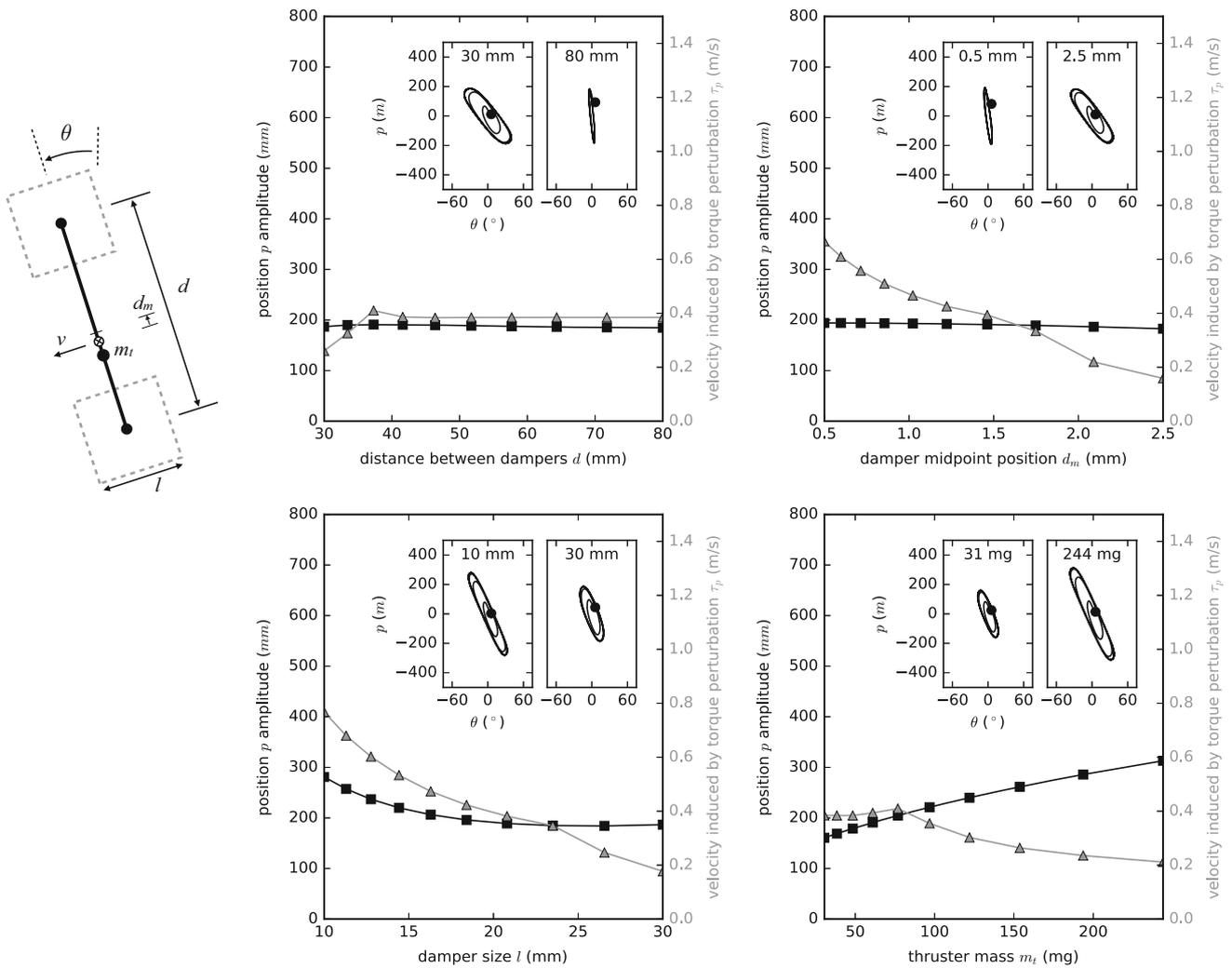
Fig. 13 Wing-free model: how varying different parameters affects the amplitude of oscillations. (*Top left*) Diagram of parameters that are varied. (*Top middle*) Position amplitude remains constant (*black squares*) as damper distance increases, though attitude oscillations are reduced. (*Inset*) This occurs because, as damper distance increases, the time of period of each oscillation increases. (*Top right*) Varying the damper midpoint position has little effect on position amplitude. (*Bottom left*) Increasing damper size reduces position oscillation, but this comes at the expense of increased weight. (*Bottom right*) Increasing thruster mass increases oscillation amplitude. (*All*) The effect of a torque disturbance. Increasing the damper midpoint position in the positive body z-direction or increasing damper size reduces the effect of torque disturbances (*Grey triangles*). Other perturbations have a smaller effect

time period of the oscillations. For the torque disturbance response, we found that increasing the damper midpoint position in the positive body z-direction or increasing damper size reduces the effect. Other perturbations have a smaller effect. This confirms the intuition that while larger dampers have the desirable effect of both reducing oscillation amplitude and increasing disturbance rejection, this comes at the cost of greater mass.

As above, we then considered how to choose parameters to reach a target attitude oscillation amplitude. Removing the effect of the wings permitted smaller oscillations, so we chose a target of a 15° amplitude. The resulting data and model were found as above in Sect. 6.1.1, with the results

shown in Fig. 14. The relation giving the necessary damper distance to achieve 15° oscillations is given by

$$d = 0.11 m_t^{0.19} l^{-0.28},$$

where m_t is given in kg and l and d are given in m. This shows that without the wings, damper distance has a much stronger effect to reduce attitude oscillations, and damper distance does not scale with mass as quickly.

For the wing-free case, parameter variations had a much larger effect on position oscillations. Accordingly, this enabled an optimization to achieve a target position amplitude. Minimizing the size of these oscillations is of interest
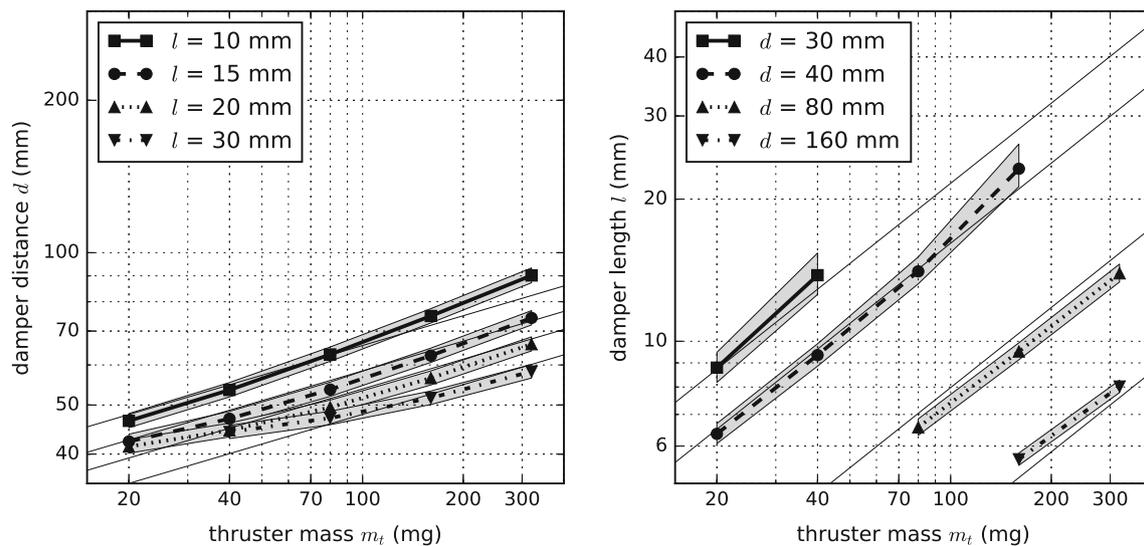
Fig. 14 Design guidelines for a damper-equipped robot without wing drag. (*Left*) The damper distance d necessary to achieve an attitude oscillation amplitude of $15°$ for different thruster masses m_t and damper length l. The *shaded area* represents variability as the target amplitude is varied by $\pm 1°$. (*Right*) The damper length l necessary to achieve a position oscillation amplitude of $6.25 \times d$ for different damper distances and thruster masses. *Shaded area* represents the variability as the amplitude target is varied by 1 mm. Data is not plotted for cases in which the model gives a damper distance that is too small to be physically possible or a damper length below 5 mm

for applications in confined spaces. But because damper distance d has no effect on position amplitude (Fig. 13), we instead optimized over the damper length l, and choosing a target amplitude of 25 cm for the case of $d = 40$ mm. The relation giving the necessary damper length to achieve the desired amplitude of position oscillations is is given by

$$l = 7.1 m_t^{0.64} d^{0.046}.$$

This shows that there is a very weak dependence on the distance between dampers as indicated by the small exponent on d as expected from Fig. 13.

We then performed an analysis aimed at finding scale-invariant properties. Between the two candidate length scales, l and d, the damper distance d is larger, so we chose it as the driving characteristic. For this analysis, we then fixed the position oscillation amplitude target to be proportional to the size of the vehicle, according to $6.25d$. This corresponds to a 25 cm amplitude for a $d = 40$ mm vehicle. The analysis is shown in Fig. 14 and the resulting relation is given by

$$l = 0.11 m_t^{0.56} d^{-1.0}. \tag{17}$$

This shows that as the damper distance increases (with other parameters held constant), the oscillation amplitude increases roughly proportion (because orbit size was fixed in proportion to d). Therefore, there are two routes to compensating for an increase in thruster mass: either increase damper distance for little gain in weight but an increase in oscilla-

tions, or increase damper length to maintain oscillation size at the cost of increased weight.

If we postulate a size scale for the thruster L such that its mass scales as L^3, then substituting L^3 for m_t in Eq. (17) (ignoring the constant scaling factor), we can see that to maintain the same-sized position oscillations, the damper's length must vary by $L^{.17}$, and therefore the damper's mass by $L^{.34}$. This indicates that the damper size and mass become proportionally smaller as the thruster size increases. Conversely, the dampers get relatively larger as scale reduces.

7 Conclusions

In this work we have presented an analysis of the aerodynamics of a damper-equipped hovering aerial vehicle at insect scale and used it to propose sizing guidelines for a range of vehicle sizes. We were able to use dampers to stabilize the attitude of an insect-sized, flapping wing vehicle during hovering flight. Without dampers or another form of feedback, this vehicle quickly crashed to the ground because of dynamic instability. The basic principle of operation is a coupled lateral-rotational dynamical system in which there is inherent self-righting. Our work builds on earlier demonstrations of the principle on larger vehicles to reveal how the dynamics of a damper-equipped vehicle vary as vehicle configuration changes.

We draw a parallel between our damper robot and how insects are thought stabilize their upright orientation. They are thought to combine self-righting through drag on the

wings with rotational damping induced by sensory feedback or fibrous appendages (Ristroph et al. 2013). Rotation sensing is thought to be mediated by the gyroscopic halteres in flies (Dickinson et al. 1999), and either vibrating antennae (Sane et al. 2007) or torsional forces in the wings in moths (Eberle et al. 2015). While it is not known how other animals such as honeybees sense rotation, flight tests on a robotic fly have been used to hypothesize that their light-sensing ocelli could perform this role (Fuller et al. 2014b).

The benefit of passive dampers is that the design of the vehicle can be made much simpler because it does not require an active sense-react feedback loop to maintain stability. Additionally, any sensor used to stabilize the dynamics of small robots must operate with a high bandwidth because of the fast dynamics at this scale (Åström and Murray 2008). This requires greater power usage. In contrast, an air-damper-equipped vehicle could forego such fast sensors, permitting a much slower feedback loop and sensors and requiring less power.

The benefit of the simplicity of dampers come with some costs. First, our results indicate that periodic oscillations cannot be avoided in this design. Periodic positional excursions with an amplitude of 20 cm are unavoidable, as are rotational oscillations of 15–30°. Secondly, the large surface area exposed to the wind by dampers may restrict flight in windy conditions, suggesting that dampers may find their best application indoors. Our results indicate that wind susceptibility can be somewhat mitigated by reducing damper area, at the cost of larger position and attitude excursions (Figs. 13, 11, bottom left). Conversely, our results indicate that only by increasing damper size can lateral position oscillation amplitude be significantly reduced. This comes at the cost of increased damper mass.

We also draw some conclusions about how dampers scale with robot size. Our results indicate that there are two routes to compensating for an increase in thruster mass: either increase damper distance for little gain in weight but an increase in position oscillation amplitude, or increase damper size to maintain oscillation size at the cost of increased weight. We also show that as robot scale L decreases (and its mass by L^3), the damper mass scales downward very slowly as $L^{.34}$ for a fixed-size position amplitude. This indicates that at small scales, the dampers must be comparatively large. Our analysis does not account for viscous friction, however, which grows with diminishing scale, so future work will investigate how this comes into play at the very smallest scales where fluid dynamics are better modeled by Stokes' flow.

Future work will attempt to perform flight control on damper-equipped robots. Our torque perturbation analysis indicates that a small torque can in all cases produce a lateral velocity, which could be used for flight control. We suggest that a reasonable first application could consist of a very simple sensor suite such as a temperature sensor and a magnetometer to sense orientation. Using only occasional sampling, it could perform a bacteria-inspired biased random walk toward sources of heat by sampling the gradient (Macnab and Koshland 1972).

References

Abzug, M. J., & Larrabee, E. E. (2002). *Airplane stability and control. A history of the technologies that made aviation possible* (2nd ed.). Cambridge: Cambridge University Press.

Åström, K. J., & Murray, R. M. (2008). *Feedback systems: An introduction for scientists and engineers*. Princeton: Princeton University Press.

Blevins, R. D. (2015). *Formulas for dynamics, acoustics and vibration*. New York: Wiley.

Chirarattananon, P. C., & Wood, R. J. (2013). Identification of flight aerodynamics for flapping-wing microrobots. In *2013 IEEE international conference on robotics and automation (ICRA)*.

De Croon, G., De Clercq, K., Ruijsink, R., Remes, B., & De Wagter, C. (2009). Design, aerodynamics, and vision-based control of the delfly. *International Journal of Micro Air Vehicles*, *1*(2), 71–97.

Dickinson, M. H. (1999). Haltere-mediated equilibrium reflexes of the fruit fly, drosophila melanogaster. *Philosophical Transactions of the Royal Society of London B*, *354*, 903–916.

Dickinson, M. H., & Götz, K. G. (1996). The wake dynamics and flight forces of the fruit fly drosophila melanogaster. *Journal of Experimental Biology*, *199*(9), 2085–2104.

Dickinson, M. H., Lehmann, F. O., & Sane, S. P. (1999). Wing rotation and the aerodynamic basis of insect flight. *Science*, *284*(5422), 1954–1960.

Dudley, R. (2002). *The biomechanics of insect flight: Form, function, evolution*. Princeton: Princeton University Press.

Eberle, A., Dickerson, B., Reinhall, P. G., & Daniel, T. (2015). A new twist on gyroscopic sensing: Body rotations lead to torsion in flapping, flexing insect wings. *Journal of the Royal Society Interface*, *12*(104), 20141,088.

Ellington, C. P. (1984). The aerodynamics of hovering insect flight. ii. Morphological parameters. *Philosophical Transactions of the Royal Society of London B, Biological Sciences*, *305*(1122), 17–40. doi:10.1098/rstb.1984.0050.

Ellington, C. P., Van Den Berg, C., Willmott, A. P., & Thomas, A. L. (1996). Leading-edge vortices in insect flight. *Nature*, *384*(19), 626–630.

Fearing, R., Chiang, K., Dickinson, M., Pick, D., Sitti, M., & Yan, J. (2000). Wing transmission for a micromechanical flying insect. In *IEEE international conference on robotics and automation (ICRA)* vol. 2, (pp. 1509–1516).

Finio, B. M., Pérez-Arancibia, N. O., & Wood, R. J. (2011). System identification and linear time-invariant modeling of an insect-sized flapping-wing micro air vehicle. In *2011 IEEE/RSJ international conference on intelligent robots and systems (IROS)*.

Fuller, S. B., Helbling, E. F., Chirarattananon, P., & Wood, R. J. (2014a). Using aMEMS gyroscope to stabilize the attitude of a fly-sized

hovering robots. In *2014 International conference on micro air vehicle (IMAV), Delft, The Netherlands*.

Fuller, S. B., Karpelson, M., Censi, A., Ma, K. Y., & Wood, R. J. (2014b). Controlling free flight of a robotic fly using an onboard vision sensor inspired by insect ocelli. *Jouranl of the Royal Society Interface*. doi:10.1098/rsif.2014.0281.

Gravish, N., Peters, J. M., Combes, S. A., & Wood, R. J. (2015). Collective flow enhancement by tandem flapping wings. *Physical Review Letters*, *115*(18), 188101.

Helbling, E. F., Fuller, S. B., & Wood, R. J. (2014). Pitch and yaw control of a robotic insect using an onboard magnetometer. In *2014 IEEE international conference on robotics and automation (ICRA)*.

Hoerner, S. F. (1965). *Fluid-dynamic drag: Practical information on aerodynamic drag and hydrodynamic resistance*. Midland Park: Hoerner Fluid Dynamics.

Keennon, M., Klingebiel, K., Won, H., & Andriukov, A. (2012). Development of the nano hummingbird: A tailless flapping wing micro air vehicle. In *AIAA aerospace sciences meeting, AIAA, Reston, VA* (pp. 1–24). doi:10.2514/6.2012-588.

Kroo, I., & Kunz, P. (2000). Development of the mesicopter: A miniature autonomous rotorcraft. In *American helicopter society (AHS) vertical lift aircraft design conference, San Francisco, CA*.

Ma, K. Y., Felton, S. M., & Wood, R. J. (2012). Design, fabrication, and modeling of the splitactuator microrobotic bee. In *2012 IEEE international conference on robotics and automation (ICRA), St. Paul, MN* (pp. 1133–1140).

Ma, K. Y., Chirarattananon, P., Fuller, S. B., & Wood, R. (2013). Controlled flight of a biologically inspired, insect-scale robot. *Science*, *340*(6132), 603–607.

Macnab, R. M., & Koshland, D. (1972). The gradient-sensing mechanism in bacterial chemotaxis. *Proceedings of the National Academy of Sciences*, *69*(9), 2509–2512.

Pérez-Arancibia, N. O., Ma, K. Y., Galloway, K. C., Greenberg, J. D., & Wood, R. J. (2011). First controlled vertical flight of a biologically inspired microrobot. *Bioinspiration and Biomimetics*, *6*(3), 036009. doi:10.1088/1748-3182/6/3/036009.

Pesavento, U., & Wang, Z. (2009). Flapping wing flight can save aerodynamic power compared to steady flight. *Physical Review Letters*, *103*(11), 118,102.

Pringle, J. W. S. (1948). The gyroscopic mechanism of the halteres of diptera. *Philosophical Transactions of the Royal Society of London Series B, Biological Sciences*, *233*(602), 347–384.

Richter, C., & Lipson, H. (2011). Untethered hovering flapping flight of a 3d-printed mechanical insect. *Artificial Life*, *17*(2), 73–86.

Ristroph, L., Bergou, A. J., Ristroph, G., Coumes, K., Berman, G. J., Guckenheimer, J., et al. (2010). Discovering the flight autostabilizer of fruit flies by inducing aerial stumbles. *Proceedings of the National Academy of Sciences*, *107*(11), 4820–4824. doi:10.1073/pnas.1000615107.

Ristroph, L., Ristroph, G., Morozova, S., Bergou, A. J., Chang, S., Guckenheimer, J., et al. (2013). Active and passive stabilization of body pitch in insect flight. *Journal of the Royal Society Interface*. doi:10.1098/rsif.2013.0237.

Sane, S. P., & Dickinson, M. H. (2001). The control of flight force by a flapping wing: Lift and drag production. *The Journal of Experimental Biology*, *204*, 2607–2626.

Sane, S. P., Dieudonné, A., Willis, M. A., & Daniel, T. L. (2007). Antennal mechanosensors mediate flight control in moths. *Science*, *315*(5813), 863–866. doi:10.1126/science.1133598.

Sreetharan, P., & Wood, R. J. (2011). Passive torque regulation in an underactuated flapping wing robotic insect. *Autonomous Robots*, *31*(2–3), 225–234.

Tanaka, H., & Shimoyama, I. (2010). Forward flight of swallowtail butterfly with simple flapping motion. *Bioinspiration & Biomimetics*, *5*(2), 026003. doi:10.1088/1748-3182/5/2/026003.

Teoh, Z. E., Fuller, S. B., Chirarattananon, P. C., Pérez-Arancibia, N. O., Greenberg, J. D., & Wood, R. J. (2012). A hovering flapping-wing microrobot with altitude control andpassive upright stability. In *2012 IEEE/RSJ international conference on intelligent robots and systems (IROS), Vilamoura, Algarve, Portugal* (pp. 3209–3216).

Trimmer, W. S. N. (1989). Microbots and micromechanical systems. *Sensors and Actuators*, *19*, 267–287.

Ulrich, E., Pines, D., & Humbert, J. S. (2010). From falling to flying: The path to powered flight of a robotic samara nano air vehicle. *Bioinspiration & Biomimetics*, *5*(045), 009.

van Breugel, F., Regan, W., & Lipson, H. (2008). From insects to machines. *IEEE Robotics & Automation Magazine*, *15*(4), 68–74. doi:10.1109/MRA.2008.929923.

Wang, Z. J., Birch, J. M., & Dickinson, M. H. (2004). Unsteady forces and flows in low reynolds number hovering flight: Two-dimensional computations versus robotic wing experiments. *Journal of Experimental Biology*, *207*(3), 449–460. doi:10.1242/jeb.00739.

Whitney, J., Sreetharan, P., Ma, K., & Wood, R. (2011). Pop-up book mems. *Journal of Micromechanics and Microengineering*, *21*(11), 115021.

Wilson, M. (1978). The functional organisation of locust ocelli. *Journal of Comparative Physiology*, *124*(4), 297–316. doi:10.1007/BF00661380.

Wood, R. J. (2008). The first takeoff of a biologically inspired at-scale robotic insect. *IEEE Transactions on Robotics*, *24*(2), 341–347. doi:10.1109/TRO.2008.916997.

Wood, R. J., Avadhanula, S., Menon, M., & Fearing, R. S. (2003). Microrobotics using composite materials: The micromechanical flying insect thorax. In *2003 ieee international conference on robotics and automation (ICRA)* (vol. 2 pp. 1842–1849). doi:10.1109/ROBOT.2003.1241863.

Wood, R. J., Avadhanula, S., Sahai, R., Steltz, E., & Fearing, R. S. (2008). Microrobot design using fiber reinforced composites. *Journal of Mechanical Design*, *130*, 052304.

Zdunich, P., Bilyk, D., MacMaster, M., Loewen, D., DeLaurier, J., Kornbluh, R., et al. (2007). Development and testing of the mentor flapping-wing micro air vehicle. *Journal of Aircraft*, *44*(5), 1701–1711.

Sawyer B. Fuller is an Assistant Professor of Mechanical Engineering at the University of Washington, Seattle. He was previously a postdoctoral scholar at the School of Engineering and Applied Sciences, Harvard University. He holds a Ph.D. in Bioengineering at the California Institute of Technology and B.S. and M.S. degrees in Mechanical Engineering at the Massachusetts Institute of Technology. In addition to his work in insect flight control, he has also developed a frog-hopping planetary exploration rover prototype at the NASA Jet Propulsion Laboratory and invented a printer to fabricate 3D microfabricated circuits and machines at the MIT Media Lab. His work encompasses forward-engineering robotics and reverse-engineering biology through scientific experiment.

Zhi Ern Teoh is a postdoctoral scholar at the School of Engineering and Applied Sciences at Harvard University. He holds a Ph.D. in Engineering Science at Harvard University, an M.S. in Aeronautical Engineering from Stanford University, and a B.S. in Mechanical Engineering from Cornell University. He investigates the mechanics and design of insect-sized aerial robots.

Jack Greenberg is Associate Product Manager at Google, Inc. He holds a B.A. in Physics at Harvard University.

Pakpong Chirarattananon is an assistant professor in the Department of Mechanical and Biomedical Engineering at the City University of Hong Kong, where he investigates biology-inspired control strategies for insect- and bird-inspired aerial robots. He holds a Ph.D. from the School of Engineering and Applied Sciences at Harvard University, and a B.S. in Physics from Cambridge University.

Robert J. Wood is the Charles River Professor of Engineering and Applied Sciences in Harvard's School of Engineering and Applied Sciences and a founding core faculty member of the Wyss Institute for Biologically Inspired Engineering. Prof. Wood completed his M.S. and Ph.D. degrees in the Department of Electrical Engineering and Computer Sciences at the University of California, Berkeley. He is founder of the Harvard Microrobotics Lab which leverages expertise in microfabrication for the development of biologically-inspired robots with feature sizes on the micrometer to centimeter scale. His current research interests include new micro- and meso-scale manufacturing techniques, fluid mechanics of low Reynolds number flapping wings, control of sensor-limited and computation-limited systems, active soft materials, and morphable soft-bodied robots. He is the winner of multiple awards for his work including the DARPA Young Faculty Award, NSF Career Award, ONR Young Investigator Award, Air Force Young Investigator Award, Technology Review's TR35, and multiple best paper awards.

Néstor O. Pérez-Arancibia is an assistant professor in the Department of Aerospace and Mechanical Engineering at the University of Southern California (USC). His current research and teaching interests include linear systems theory, nonlinear and adaptive control, biologically-inspired robotics, and mechatronics. He holds a Ph.D. in Mechanical Engineering from the University of California, Los Angeles (UCLA).